

TWI EXPERIMENTAL RESULTS BY A LINEAR INVERSE SCATTERING APPROACH

R. Solimene, A. Brancaccio, and R. Pierri

Dipartimento di Ingegneria dell'Informazione
Seconda Unviersita' di Napoli
via Roma 29, Aversa 81031, Italy

F. Soldovieri

Istituto per il Rilevamento Elettromagnetico dell'Ambiente
Consiglio Nazionale delle Ricerche
via Diocleziano 328, Napoli 80124, Italy

Abstract—A *through-wall imaging* problem is tackled by means a linear inverse scattering approach described and numerically analyzed in previous works by the same authors. Here, such an approach is checked for against experimental data. To this end, a CW-SF ultra-wideband radar system is used to take measurements in a controlled environment as well as for in situ experiments. Different types of scatterers and of obscuring walls are considered.

1. INTRODUCTION

The development of imaging algorithms to *see-through* an obscuring obstacle is now addressed in the scientific literature as a *through-wall imaging* (TWI) problem. Such a research field has been receiving increasing interest since many civilian and law enforcement scenarios require tackling the problem of detecting and localizing objects which are hidden behind a wall [1–5].

For example, a typical scattering scenario for TWI is the search for hostage and suspects located inside a building [6].

As electromagnetic waves can propagate through nonmetallic building materials, such a task is in principle possible by adopting radar systems [7]. However, even though TWI shares most of the scientific/technical aspects of free-space imaging, it is definitively more

Corresponding author: R. Solimene (raffaele.solimene@unina2.it).

difficult from an applicative point of view due to the presence of the wall [6].

First, the attenuation the electromagnetic waves undergo while propagating through the wall set an upper limit to the exploitable frequencies. Experimental observations have shown that most of the building materials are relatively *transparent* up to 2–3 GHz and for higher frequencies the attenuation begins to increase rapidly [8, 9].

Second, the imaging algorithms have to account for the propagation path through the wall, otherwise blurred images are obtained where the scatterers appear distorted and dislocated from their actual positions.

In order to comply with the above mentioned constraints different TWI algorithms have been developed. For example, in [10] a beamforming algorithm is exploited, in [11] a chaos modulation imaging technique is adopted whereas in [3] and [12] the reconstruction approaches are based on nonlinear and linear inverse scattering theory, respectively.

In this paper, we present the experimental validation of the linear inverse scattering approach described in [12]. In fact, the experimental validation is a mandatory step towards the definitive assessment of the effectiveness of any imaging scheme.

We first test the imaging algorithm by means of measurements taken in a semi-anechoic controlled environment. Then we consider in situ scattering experiments under realistic conditions.

In particular, the measurements are taken thanks to a portable ultra-wideband continuous wave stepped frequency (CW-SF) radar.

The paper is organized as follows. In Section 2, we describe the geometry of the problem, the measurement configuration and briefly recall the imaging algorithm. In Section 3, we introduce the adopted instrumentation. Section 4 is devoted to showing the experimental results. Finally, conclusions end the paper.

2. SCATTERING CONFIGURATION AND IMAGING ALGORITHM

Figure 1 depicts the reference scenario used to develop the scattering model upon which the imaging algorithm is based. The TWI problem is addressed by considering a simple “background” medium consisting of three layers. The first and the third ones are assumed free-space and their dielectric permittivity and magnetic permeability are denoted as ϵ_0 and μ_0 , respectively.

The second layer represents the wall. Such a layer is assumed homogeneous and nonmagnetic (i.e., its magnetic permeability is the

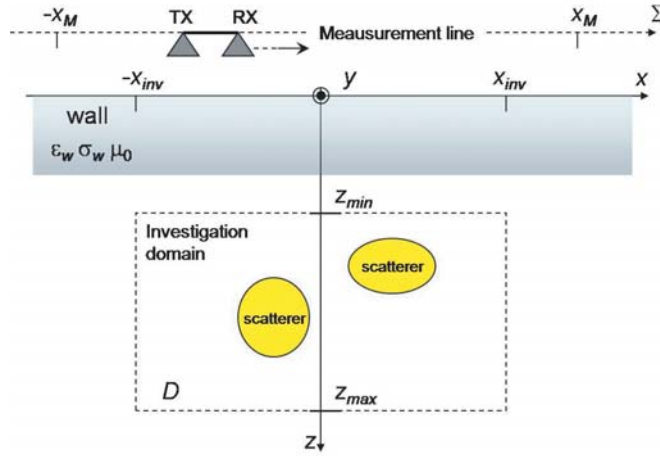


Figure 1. Geometry of the problem.

same as the one of the free-space) with ϵ_w and σ_w denoting its dielectric permittivity and conductivity, whereas d is its thickness.

As dictated by the TWI problem, the scatterers and the antennas are located on the opposite sides of the wall. In particular, the transmitting (TX) as well the receiving (RX) antennas are located in the first layer whereas the targets are located in the third layer. A measurement aperture $\Sigma = [-x_M, x_M]$ is synthesized at a given standoff distance h from the wall. More in detail, the TX and RX are separated by a fixed offset so that measurements are collected at a fixed distance from the source while the latter moves. For each source position measurements are taken at different frequencies within a frequency band $f \in [f_{\min}, f_{\max}]$. Accordingly, a *multibistatic/multi-frequency* configuration is achieved.

The targets are assumed to be infinitely long and invariant along the y -axis whereas the sources of the incident field are modeled as a filamentary current directed along the same axis. Therefore, we develop the TWI imaging algorithm for a two-dimensional scalar geometry. Finally, we assume that the targets are located within an investigation domain $D = [-x_{\text{inv}}, x_{\text{inv}}] \times [z_{\text{min}}, z_{\text{max}}]$.

Under the Born approximation the imaging problem amounts to inverting the following integral relationship [13]

$$E_S(x_O, f) = H(f) \iint_D G(x_O, x, z, f) E_{\text{inc}}(x, z, f) \chi(x, z) dx dz, \quad (1)$$

where $H(\cdot)$ is a slowly varying function of f , $x_O \in \Sigma$ is the observation position, $G(\cdot)$ is the Green's function pertinent to the addressed three-

layered background medium and $E_{\text{inc}}(\cdot)$ is the field impinging on the scatterers, that is the field radiated by the elementary source and transmitted in the third layer beyond the wall. $E_S(\cdot)$ is the datum of the problem and represents the field scattered by the objects which propagates through the wall (in the direction opposite to the one of E_{inc}) and collected over the measurement aperture Σ . Whereas the unknown is given by the so-called contrast function $\chi(\cdot)$ which represents the unknown scatterers in terms of the relative difference between the background dielectric permittivity, in this case ϵ_0 , and the objects one $\epsilon_o b_j(\cdot)$, that is $\chi(\cdot) = \epsilon_o b_j(\cdot)/\epsilon_0 - 1$ [13–15]. The Born model works for the so-called weak scatterers. However, it is shown that it allows to obtain *qualitative* information about the location and the geometrical features of the scatterers even for the case of metallic objects [12].

It is important to note that in Eq. (1) the data of the problem (hereinafter addressed as the scattered field) are given in terms of the difference between the total scattered field (i.e., the actual measurements which consist of the field reflected by the wall plus the field scattered by the obscured objects) and the background field (i.e., the field reflected by the wall only). This means that before inverting Eq. (1) the scattered field $E_S(\cdot)$ has to be derived from the measurements. This requires the knowledge of the wall parameters or their estimation [16]. The knowledge of the wall is also necessary to define the kernel of the operator in Eq. (1) to be inverted.

Here, however, we assume to know the wall parameters.

According to the previous discussion, once the scattered field has been obtained, the reconstruction problem consists in solving eq. (1) for the contrast function $\chi(\cdot)$. As is well known, this entails tackling an ill-posed problem [17]. In particular, as the integral operator in eq. (1) is compact even a small amount of noise on data can result in a completely meaningless reconstruction. In order to build up an inversion scheme which is robust against noise one must establish a trade-off between accuracy and stability. In other words, a regularization scheme has to be adopted. Here, we adopt the truncated-singular value decomposition (TSVD) inversion scheme. Thus, a regularized solution of the integral Eq. (1) is obtained as

$$\mathcal{R}\chi = \sum_{n=0}^N \frac{\langle E_S, v_n \rangle}{\sigma_n} u_n, \quad (2)$$

where $\mathcal{R}\chi$ is the regularized reconstruction, N is the truncation index, the set $\{\sigma_n\}_{n=0}^{\infty}$ denotes the singular values ordered in a non increasing sequence, whereas $\{u_n\}_{n=0}^{\infty}$ and $\{v_n\}_{n=0}^{\infty}$ form orthonormal bases in the unknown and data spaces, respectively [17]. The TSVD



Figure 2. Picture of the scattering experiment in a semi-anechoic environment.

achieves regularization by reducing the unknown functional space dimension. Accordingly, the key question is the choice of truncation index N which has to be done by accounting for the noise level, the mathematical features of the operator to be inverted and available a priori information about the unknown. Different methods exist to select N . Such methods can explicitly exploit the knowledge of the noise level, (such as the Morozov discrepancy principle) or not (such as the generalized cross validation) [18]. In general, the higher the noise the lower N . For the problem at hand, the singular values decay with an exponential law beyond a certain index. This is shown analytically, for example, for the one-dimensional case in [4] but approximately also holds for the two-dimensional case. Indeed, this reflects the fact that the scattered field has finite number of degrees of freedom [19]. Therefore, when the noise is white, it is natural to set the truncation index roughly in correspondence to the index where the singular values start to decay quickly. In the following we will adopt such a criterion. In particular, a visual inspection of the singular value behaviour suggests to retain in eq. (2) the singular functions corresponding to the singular values not below 20dB the maximum one.

3. RADAR SYSTEM

In this section, we briefly describe the instrumentation we adopted to collect measurements. We used a portable continuous wave stepped frequency radar system (see Fig. 2) developed and implemented under a cooperation between the Second University of Naples and Ingegneria

dei Sistemi [20]. The main components of such a system are the electronic unit, the automatic positioning system and the antennas. The data acquisition procedure is supervised by a laptop via a USB port thanks to a customized software written in Labview language. In particular, the software permits to choose the number and the step of the working frequencies, the radiated power and the number and spacing of the spatial measurement as well as the kind of acquisition.

The electronic unit is made up of a transmitter and two receiving channels which work in the frequency 800 MHz–4 GHz band. The maximum number of frequencies that can be taken is 3200. Hence a minimum frequency step of 1 MHz is allowed. Each single frequency measurement requires roughly 1 ms. The I and Q components of the signal are acquired. The maximum transmitter power is 0 dBm. The electronic unit permits to control three antennas, one transmitting and two receiving. The antennas are automatically positioned thanks to a slide driven by a stepped motor. The slide is 2.5 m long and allows a measurement line of 2 m at most. The offset between the antennas is fixed but it can be adjusted manually at any desired value between 10 cm and 1 m.

In the following experiments we used only two antennas (one acting as transmitting one and the other as receiving one), two rectangular ridged horns (Schwarzbeck mod. BBHA9120A) which can work between 800 MHz and 5 GHz, linearly polarized along the y -axis.

A more detailed description of the hardware system can be found in [20].

4. EXPERIMENTAL RESULTS

This section is devoted to showing some experimental reconstructions in order to assess the reconstruction capabilities of the inversion algorithm. In particular, the reconstructions are given first for a scattering scenario within a semi-anechoic environment and after for in situ experiments.

The imaging problem for realistic situations is intrinsically a three-dimensional problem. However, for the sake of simplicity, we perform the reconstructions according to the reference scenario and the measurement configuration described in Section 2. In other words we assume to deal with a two-dimensional and scalar problem and thus the results will be presented in terms of a two-dimensional slice of the scene.

In particular, for all the following reconstructions the modulus of the regularized retrieved contrast function normalized to its maximum, that is $|R\chi(x; z)|/\max|R\chi(x, z)$ is displayed.

4.1. Calibration

Before proceeding to the reconstructions, the radar system must be calibrated to remove the systematic errors due to the radar circuitry, the cables, the cable-antenna transitions and to the antennas. Indeed, from the actual measurements concerning the scattering parameter S_{21} the scattered field has to be obtained.

As to the radar system, the coherence loss is due to the different electrical path that different sub-bands of the received signal experience. This is because the different sub-bands share only part of the internal circuitry. To compensate for such an effect the system includes a phase auto-calibration circuit. Such a circuit requires first to acquire a full CW-SF scan in a controlled path, then the successive scans are calibrated using this data to correct phase misalignment. Moreover, the information acquired during the calibration process allows a complete equalization of the subsystems in terms of phase and amplitude. The calibration process is completely automated and repeated at regular intervals during measurements, allowing the effect of system thermal drift to be tracked and corrected.

After such an automatic internal calibration, the path through the cables and the antennas still remains to be compensated for. To this end, measurements collected for a copper plate scatterer located at a known distance from the antennas are exploited. In particular, the plate distance is chosen so that the reflection coming from the copper plate is easily discernable from the antennas' direct coupling. This allows us to estimate the *time-position* (after a Fourier transformation as data are in the frequency domain) of the plate, and hence, as the free-space path is known, the cable-antenna path length z_{ca} is determined. Therefore, the scattered field is approximated simply as

$$E_S(x_O, f) = S_{21} \exp(j4\pi f z_{ca}/c), \quad (3)$$

c being the speed of light in free-space.

Note that the antennas' frequency behavior is not accounted for by the calibration stage. According to Section 2, all the following results will be achieved by assuming a two-dimensional filamentary current as antenna in the model.

4.2. Experiments in Controlled Environment

The set up of the first experiment is shown in Fig. 2.

It refers to the case of two hollow metallic cylinders of 2 m in height with circular cross sections of diameters 10 cm and 6 cm, respectively, whose centers are located at a depth of $z = 40$ cm (with respect to the reference system reported in Fig. 1) that is at about 30 cm from the

second interface of the wall. Such scatterers are located behind a tuff wall of size $1 \times 1 \times 0.11 \text{ m}^3$ (0.11 m being the thickness). The dielectric permittivity and conductivity of the tuff wall are assumed known in the imaging algorithm. In particular, we set $\epsilon_w = 4\epsilon_0$ according to the outcome of the electromagnetic characterization procedure reported in [19]. The dispersive nature of the tuff as well as its losses are not considered in the inversion model.

The radar system is placed in front the wall so that the antennas are at 10 cm apart from the first wall interface. The measurements exploited in the inversion range from 800 MHz to 3200 MHz with a frequency step of 60 MHz. Moreover, a synthetic aperture $\Sigma = [-0.5, 0.5] \text{ m}$ has been synthesized where the scattered field is collected at a spatial step of 2.5 cm.

Finally, the scattering scene is located in a semi-anechoic environment where three sides of the room are covered with absorbing panels $2.5 \times 2.5 \text{ m}^2$ sized.

As to the imaging algorithm, an investigation domain $D = [-0.5, 0.5] \times [0.11, 1] \text{ m}^2$ has been assumed and the TSVD truncation index N , in Eq. (2), is chosen so as to retain the singular functions corresponding to the singular values not below 20 dB of the maximum one. It is worth remarking that only half of the measurements are exploited in the imaging algorithm. That is, for imaging purposes, we retain in the inversion only the measurements collected at a spatial step of 5 cm. Thus, the numerical procedure is computationally more effective and it is possible by resorting to the results concerning the degrees of freedom of the scattered field [20].

According to the previous discussion two different sets of data have been acquired in presence (total scattered field) and in absence of the scatterers (background field) so that the scattered field is obtained as their difference. The results concerning a two-dimensional slice taken at an height of about 0.35 m are reported in Fig. 3. In particular, in panel (a) of such a figure the time-domain normalized amplitude of the scattered field is reported as a function of the receiving antenna's position (i.e., the so-called radargram) and obtained by Fourier transforming, for each trace, the frequency domain measurements collected by the radar system with a 1 MHz frequency step. As can be seen, the visual inspection of such a figure makes a user aware only of the scatterers presence and little else. Note that the radargram has been obtained from non-calibrated data which only entails a shifting along the depth. Instead, the tomographic reconstruction reported in panel (b), obtained from calibrated data, is definitively better as the number and the locations of the scatterers can be clearly discerned (even though the antennas' behavior as well as the tuff dispersive law

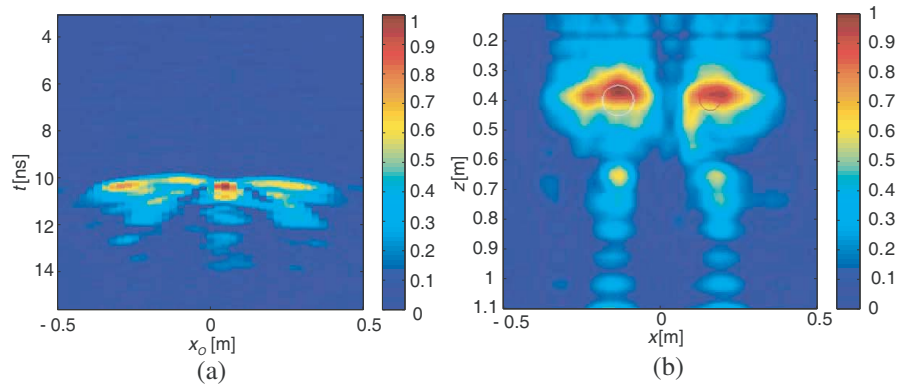


Figure 3. (a) Radargram (non-calibrated normalized amplitude Fourier transformed data), (b) image obtained by the imaging algorithm, the actual scatterers' cross sections are also depicted as white and red circles.



Figure 4. Picture of the in situ scattering experiment.

have been not accounted for).

4.3. In Situ Experiments

As a second example we go on to consider a more realistic scenario (see Fig. 4) in order to check the imaging algorithm in very realistic conditions. For such a case we placed the radar system so that the antennas are about 1 cm away from the wall. In particular, an external bearing wall of the ground floor of one of the buildings of the Faculty of Engineering of the Second University of Naples has been chosen to perform the experiments. The scatterers to be imaged are located

outside the building on the opposite side of the wall (see panels (a) of Figs. 6 and 7).

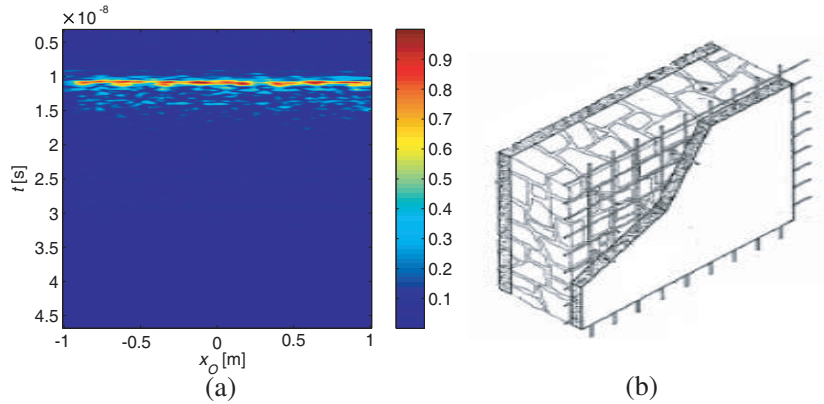


Figure 5. (a) Radargram (non-calibrated normalized amplitude Fourier transformed data), (b) pictorial view of the reinforcing grid.

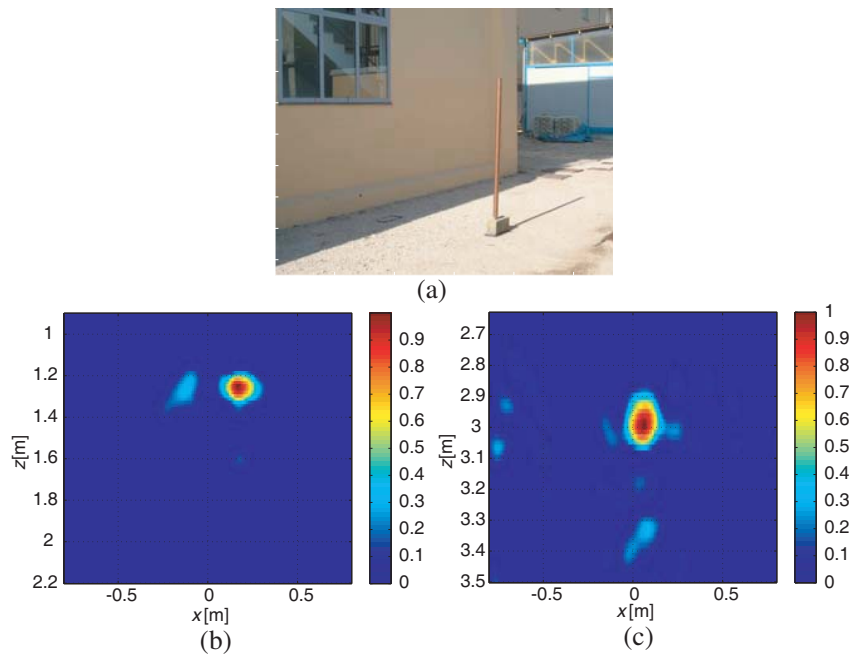


Figure 6. (a) Picture of the scattering scene, (b) reconstruction of a metallic cylinder located at 1 m behind the wall, (c) reconstruction of a metallic cylinder located at about 2.6 m behind the wall.

The measurements exploited in the inversion range from 800 MHz to 3200 MHz with a frequency step of 1 MHz, over an aperture of 2 m with a spatial step of 2 cm and at an height of 0.74 cm from the floor.

We know that the wall is made of tuff. Moreover, at the height measurements are taken, the wall is 24 cm thick. Accordingly, in the imaging algorithm we adopted $\epsilon_w = 4\epsilon_0$ and $d = 24$ cm. As in the previous case, the wall conductivity and dispersion law have not considered in the inversions.

As can be seen from Figs. 4 and 6 the scattering scenario is rather complex. The wall has a non-homogeneous thickness and above the place where the radar system is located there is a window. In this case it is also interesting to have a look at the radargram reported in Fig. 5 panel (a). The radargram reveals the existence of a periodic distribution of scatterers inside the wall which should be strong because the wall interfaces are not visible. Some information about the wall structure confirmed that a steel reinforcing grid (see Fig. 5 panel (b) for a pictorial view of the grid) was present inside the wall.

However, we do not account for the reinforcing grid in the imaging algorithm still retaining the scattering model of Section 2. Moreover, the scattered field data are again obtained as the difference from the total field and the background one.

As in the previous case, while achieving the reconstruction we consider measurements taken at a double the spatial step (i.e., at 4 cm) used to obtain the radargrams. Furthermore, a measurement line $\Sigma = [-0.8, 0.8]$ m, shorter than the one adopted for the radargram, is used. Finally, the data are also decimated in frequency. That is, we consider a frequency band $[1, 2.5]$ GHz sampled at a step of 75 MHz. This assures that waves penetrate through the grid and are not too affected by the attenuation introduced from the wall.

Finally, in all the following reconstructions the TSVD has been truncated at the same level as done for the previous test-case.

The first in situ experiment concerns the case of a hollow metallic cylinder of circular cross section with a diameter of 6 cm (see Fig. 6 panel (a)). In such a figure we consider two different situations. In panel (b), the cylinder center is located at $[0.18, 1.24]$ m, that is at 1 m beyond the wall, and an investigation domain $D = [-0.8, 0.8] \times [0.9, 2.2]$ m² is assumed. In panel (c), the cylinder is located at a greater distance from the wall $[0.03, 3]$ m, that is at about 2.6 m from the wall, and an investigation domain $D = [-0.8, 0.8] \times [2.65, 3.5]$ m² is exploited in the imaging algorithm. As can be seen, in both cases the scatterer is detected and almost correctly localized despite all the assumption upon which the inversion scheme relies on.

As a final example we consider the case of a human being as

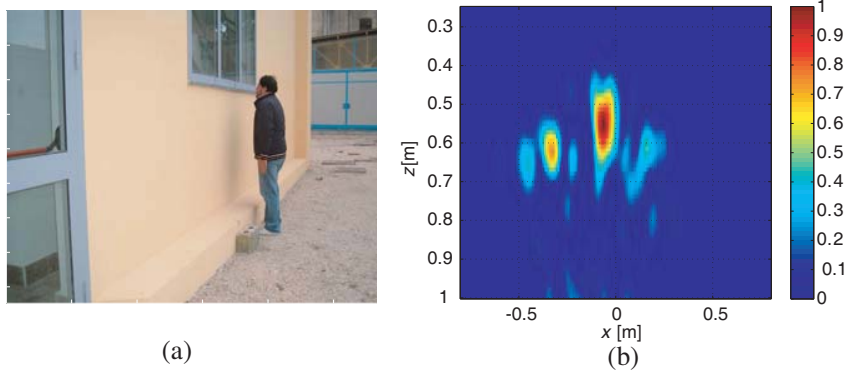


Figure 7. (a) Picture of the scattering scene in the case of human scatterers, (b) corresponding tomographic reconstruction.

scatterer (see Fig. 7 panel (a)). In particular, the center of such a scatterer is roughly located at 30 cm from the wall and slightly shifted to the left with respect to the center of the measurement line.

According to the reference frame depicted in Fig. 1 the scatterer's location is about $[-0.1, 0.55]$ m. For such an example we consider an investigation domain $D = [-0.8, 0.8] \times [0.25, 1]$ m². The corresponding reconstruction reported in the same figure in panel (b) shows that the imaging algorithm works well in detecting and localizing this scatterer as well.

5. CONCLUSIONS

We have tackled a TWI problem for scattering objects hidden by a known wall layer. As through-wall imaging has a great relevance in a number of different applicative contexts, many imaging algorithms are being developed. However, to assess the performance that an imaging algorithm can actually achieve it is mandatory to validate it against experimental data in particular for realistic scenarios.

This is just the aim we have pursued in this paper. In particular, we have checked the imaging algorithm based on an inverse scattering approach we have presented in [12] against experimental data collected both in a controlled environment and on in situ experiments.

It is shown that the proposed imaging algorithm is able to detect and localize the scatterers even in complex scattering scenarios whose features are not completely accounted for by the adopted model.

ACKNOWLEDGMENT

Effort sponsored by the Air Force Office of Scientific Research, Air Force Material Command, USAF, under the grant number FA8655-08-1-3055. The U.S. Government is authorized to reproduce and distribute reprints for Governmental purpose notwithstanding any copyright notation thereon.

REFERENCES

1. Ferris, D. D. and N. C. Currie, "A survey of current technologies for through-wall-surveillance (TWS)," *Proceedings of SPIE*, Vol. 3577, 62–72, 1999.
2. Frazier, L., "MDR for law enforcement," *IEEE Potent.*, Vol. 16, 23–26, 1998.
3. Song, L. P., C. Yu, and Q. H. Liu, "Through-wall imaging (TWI) by radar: 2-D tomographic results and analyses," *IEEE Trans. Geosci. Remot. Sens.*, Vol. 43, 2793–2798, 2005.
4. Soldovieri, F., R. Solimene, A. Brancaccio, and R. Pierri, "Localization of the interfaces of a slab hidden behind a wall," *IEEE Trans. Geosci. Remot. Sens.*, Vol. 45, 2471–2482, 2007.
5. Baranoski, E. J., "Through-wall imaging: Historical perspective and future directions," *J. Frank. Inst.*, Vol. 345, 556–569, 2008.
6. Withington, P., H. Fuhler, and S. Nag, "Enhancing homeland security with advanced UWB sensors," *IEEE Microw. Mag.*, Vol. 4, 51–58, 2003.
7. Frazier, L. M., "Surveillance through walls and other opaque materials," *IEEE National Radar Conference*, 27–31, 1996.
8. Yang, Y. and A. E. Fathy, "See-through-wall imaging using ultra wideband short-pulse radar system," *IEEE Antennas and Propagation Society International Symposium*, 334–337, 2005.
9. Hunnt, A. R., "Image formation through walls using a distributed radar sensor array," *Proceedings of the 32nd Applied Imagery Pattern Recognition Workshop (AIPR'03)*, IEEE, 2003.
10. Ahmad, F., M. G. Amin, and S. A. Kassam, "Synthetic aperture beamformer for imaging through a dielectric wall," *IEEE Trans. Aerosp. Electr. Systm.*, Vol. 41, 271–283, 2005.
11. Venkatasubramanian, V. and H. Leung, "A novel chaos-based high-resolution technique and its application to through-the-wall imaging," *IEEE Sign. Process. Lett.*, Vol. 12, 528–531, 2005.
12. Soldovieri, F. and R. Solimene, "Through-wall imaging via a linear

- inverse scattering algorithm,” *IEEE Geosc. Rem. Sens. Lett.*, Vol. 4, 513–517, 2007.
13. Chew, W. C., *Waves and Fields in Inhomogeneous Media*, IEEE Press, Piscataway, NJ, 1995.
 14. Caorsi, S., M. Donelli, A. Lommi, and A. Massa, “Location and imaging of two-dimensional scatterers by using a particle swarm algorithm,” *Journal of Electromagnetic Waves and Applications*, Vol. 18, 481–494, 2004.
 15. Huang, C. H., Y. F. Chen, and C. C. Chiu, “Permittivity distribution reconstruction of dielectric objects by a cascaded method,” *Journal of Electromagnetic Waves and Applications*, Vol. 21, 145–159, 2007.
 16. Ahamd, F., M. G. Amin, and G. Mandapati, “Autofocusing of through-the-wall radar imagery under unknown wall characteristics,” *IEEE Trans. Imag. Process.*, Vol. 16, 1785–1795, 2007.
 17. Bertero, M. and P. Boccacci, *Introduction to Inverse Problems in Imaging*, Institute of Physics, Bristol, UK, 1998.
 18. Hansen, P. C., J. G. Nagy, D. P. O’Leary, *Deblurring Images: Matrices, Spectra, and Filtering*, SIAM, 2008.
 19. Porter, R. P. and A. J. Devaney, “Generalized holography and computational solutions to inverse source problems,” *J. Opt. Soc. Am. A*, Vol. 72, 1707–1713, 1982.
 20. Parrini, F., M. Fratini, M. Pieraccini, C. Atzeni, G. De Pasquale, P. Ruggiero, F. Soldovieri, and A. Brancaccio, “ULTRA: Wideband ground penetrating radar,” *Proc. of European Radar Conference EURAD 2006*, Manchester, UK, Sep. 2006.
 21. Brancaccio, A., F. Soldovieri, G. Leone, D. Sglavo, and R. Pierri, “Microwave characterization of materials in civil engineering,” *Proc. European Microwave Assoc.*, Vol. 6, 128–135, 2006.